J. Fluid Mech. (2006), *vol.* 554, *pp.* 371–392.
doi:10.1017/S0022112005008098 Printed in the United Kingdom

Nonlinear evolution of hydrodynamically unstable premixed flames

By Y. RASTIGEJEV AND M. MATALON

Department of Engineering Sciences and Applied Mathematics, McCormick School of Engineering and Applied Science, Northwestern University, Evanston, IL 60208-3125, USA

(Received 1 March 2005 and in revised form 18 August 2005)

The nonlinear evolution of hydrodynamically unstable flames is studied numerically within the context of a hydrodynamic model, where the flame is confined to a surface separating the fresh mixture from the hot combustion products. The numerical scheme uses a variable-density Navier–Stokes solver in conjunction with a level-set front-capturing technique for the numerical treatment of the propagating front. Unlike most previous studies that were limited to the weakly nonlinear Michelson–Sivashinsky equation valid for small density changes, the present work places no restriction on the density contrast and thus elucidates the effect of thermal expansion on flame dynamics. It is shown that the nonlinear development leads to corrugated flames with a transverse dimension that is significantly larger than the wavelength corresponding to the most amplified disturbance predicted by the linear theory, and which is determined by the overall size of the system. The flame structure consists of wide troughs and relatively narrow cusp-like crests, and propagates 'steadily' at a constant speed, larger than the speed of a planar flame. The propagation speed increases as the cells widen, but eventually reaches a constant value that remains independent of the mixture's composition and of the transverse length. The dependence of the incremental increase in speed on thermal expansion is found to be nearly linear; for realistic values of thermal expansion it may be as large as 15% to 20%. In sufficiently large domains the dynamics is found to be extremely sensitive to background noise that may result, for example, from weak turbulence. Small-scale wrinkles appear sporadically on the flame surface and travel along its surface, causing a significant increase in the overall speed of propagation, up to twice the laminar flame speed.

1. Introduction

Premixed flames appear typically as corrugated surfaces with relatively sharp edges pointing towards the burnt gas; see for example figure 1 showing the image of a wrinkled methane–air inverted conical flame (known also as a V-flame) taken by Sattler, Knaus & Gouldin (2002). The image is bright in the reactants, as a result of Mie scattering of laser light off the micrometre-sized silicone oil droplets that were added to the fresh mixture and consumed in the flame zone, and dark in the products. The photograph illustrates the formation of a corrugated flame front separating burnt from unburnt gas with a cusp-like structure. The appearance of sharp folds and creases in the flame front, and the wrinkling observed over the surface of large expanding flames (Palm-Leis & Strehlow 1969; Ivashchenko & Rumyantsev 1978; Bradley, Cresswell & Puttock 2001) are manifestations of the hydrodynamic instability, discovered independently over half a century ago by Darrieus (1938) and

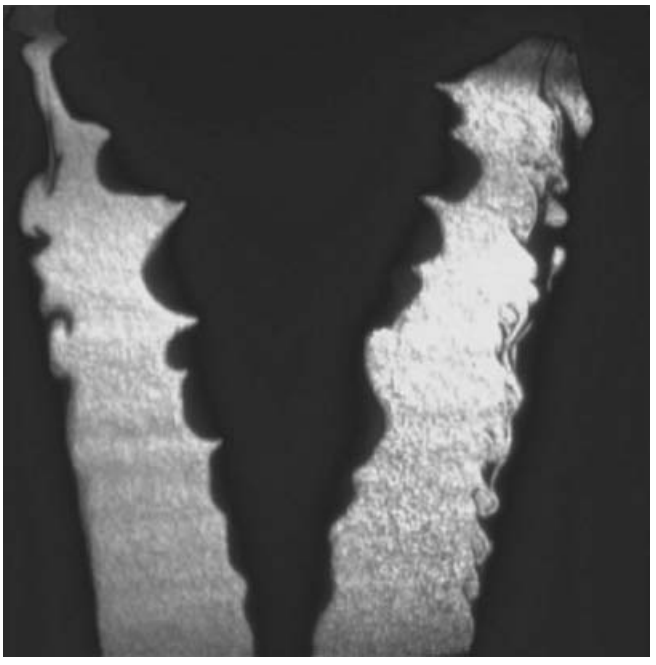

FIGURE 1. Image of a wrinkled methane–air V-flame in a turbulent flow of low intensity, showing a wrinkled flame surface with cusp formation. The image is bright in the reactants, due to Mie scattering off silicone oil droplets that were added to the fresh mixture and consumed within the flame, and dark in the products. Courtesy of F. Gouldin.

Landau (1944). The hydrodynamic instability, which results from the large change in density between the fresh mixture and the hot combustion products, implies that planar flames are unconditionally unstable, and that wrinkles of short wavelength grow faster than wrinkles of long wavelength. This result, however, is inadequate for short-wavelength disturbances that are comparable with the flame thickness, because these may induce distortions of the flame structure that were not accounted for in the Darrieus–Landau description. Much work has been done over the years to incorporate the effects of the diffusion processes within the flame zone in the analysis and clarify their stabilizing influences. Notable are the study by Markstein (1964) who assumed a dependence of the flame speed on the local curvature of the front through a phenomenological coefficient that has become known as the Markstein length, and the more rigorous asymptotic analysis of Pelce & Clavin (1982) and Matalon & Matkowsky (1982) that clarified the role of thermal, mass and viscous diffusion in stability by deriving a dispersion relation with an explicit dependence on all relevant physicochemical parameters.

The nonlinear development of a hydrodynamically unstable flame is important to understanding the structure and dynamics of fast enough and large-scale flames, where diffusion effects play a limited role. Unlike the more common cellular flames that depend on the mixture composition and have a characteristic size proportional to the wavelength of the most amplified disturbance of linear theory, hydrodynamically unstable flames have typically much larger cell sizes controlled by the overall dimension of the system. Lind & Whitson (1977) performed experiments on large expanding flames using lean hydrocarbon–air mixtures in 5–10 m thin plastic hemispherical bags, which tore loose at the early stage of propagation leaving the

flame to expand freely at nearly constant pressure. The flame first appeared as a blue expanding hemisphere, but as its size increased it became rough, with a 'pebbled' appearance. Cell sizes of approximately 10–50 cm were observed with the propagation speed increasing to 1.6–1.8 times the laminar flame speed.

Computational simulations of the Navier–Stokes equations for a multi-component chemically reacting mixture in large domains and over sufficiently long time have met significant difficulties, so that progress has relied primarily on analytical and numerical studies of simplified models. One such model is the Michelson–Sivashinsky (MS) equation obtained in the weakly nonlinear long-wave asymptotic limit (Sivashinsky 1977; Michelson & Sivashinsky 1977). The MS model is valid when the heat release is small, relative to the thermal energy of the fresh mixture namely for values of the thermal expansion coefficient $\sigma \sim 1$. Although it provides valuable physical insight in the nonlinear development of the Darrieus–Landau instability, its application is limited by the fact that $\sigma \approx 6{-}8$ for real gas mixtures. There have been attempts to extend the MS model by including higher-order terms (e.g. Bychkov 1998; Kazakov & Liberman 2002), but these studies did not produce results that are significantly different. There have also been a few numerical studies concerned with the Darrieus–Landau instability (Denet & Haldenwang 1995; Kadowaki 1999), but these were mostly concerned with the initial development of the instability.

In this paper we numerically investigate the nonlinear development of hydrodynamically unstable freely propagating flames for realistic values of σ, within the context of a hydrodynamic theory. In the hydrodynamic theory (Matalon & Matkowsky 1982; Matalon, Cui & Bechtold 2003), the whole flame associated with the region where chemical reaction, diffusion, heat conduction and viscous effects take place is assumed to be thin when compared to the representative fluid-flow length-scale associated, for example, with the size of the wrinkles on the flame front. The flow field is then determined by solving the incompressible hydrodynamic equations on each side of the resulting flame sheet, with different densities for the burnt and unburnt gases. By resolving the internal structure of the flame on the smaller diffusion scale, appropriate jump conditions for the pressure and velocities across the sheet, as well as an equation for the flame speed, are obtained as matching conditions. The resulting model is a nonlinear free-boundary problem supplemented by conditions that describe influences of the diffusion processes within the flame zone and an equation that describes the instantaneous shape and position of the flame sheet. Because of its simplicity, and the smaller number of parameters involved, the model permits the description of multi-dimensional flames with sufficient accuracy over a wide range of conditions. Furthermore, the simulations can be carried out on a uniform grid containing a moderate number of points, which reduces the computational cost significantly. We note that the complete governing equations contain a larger number of parameters and, since the flame zone is normally a few orders of magnitude smaller than the hydrodynamic length, a proper and accurate description of multi-dimensional flames by direct numerical simulation would require a prohibitively large number of points. This would also generate the need to use a sophisticated adaptive gridding technique, the development of which is a challenge in itself.

The numerical scheme employed here for simulating the evolution of multi-dimensional flames based on a hydrodynamic model was recently proposed by Rastigejev & Matalon (2006). It has already been tested on a number of benchmark problems and shown to be stable and accurate. The results presented here further show that for $\sigma - 1 \ll 1$ the predictions of the full nonlinear model are in quantitative agreement with those obtained by the weakly nonlinear model of the MS equation,

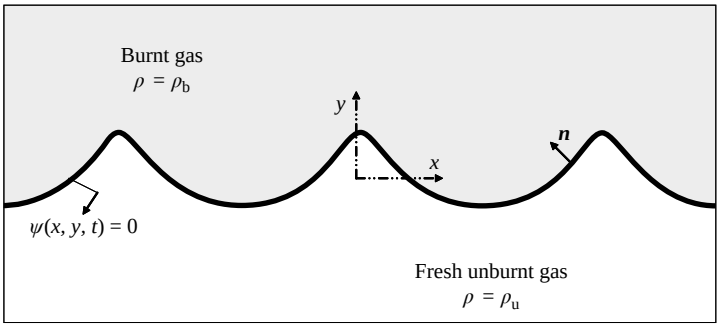

FIGURE 2. The flame as a surface of density discontinuity; the illustration corresponds to a periodically extended pole solution of the MS equation.

but our main objective is to investigate the dynamics of flame fronts with no restriction imposed on the density contrast, thus elucidating the effect of thermal expansion on flame dynamics. We show that the consequence of the hydrodynamic instability is the formation of steady-propagating cusp-like structures that resemble the experimentally observed flame fronts of figure 1. Short-wavelength corrugations introduced through initial disturbances tend to merge forming a single peak structure, whose scale is controlled by the overall size of the system. In moderate-size domains, these structures remain stable and propagate significantly faster than a planar flame does. In large domains, although a cusp-like structure develops on the average, small random subwrinkles appear sporadically on the flame sheet propagating along its surface and affecting its overall speed. Non-steady pebble-like structures have indeed been observed on the surface of large-scale flames (Istratov & Librovich 1969; Groff 1982; Bradley 1999). It is argued that these secondary structures do not represent a self-sustained phenomenon, but rather are a peculiar response to an ever-present background noise (e.g. numerical). External noise supplies small disturbances which are rapidly magnified by the hydrodynamic instability, giving rise to the small-scale wrinkles that contaminate the flame surface. Evidence of this conjecture is presented in the reported simulations.

The paper is organized as follows. A brief description of the hydrodynamic model is given in § 2. A summary of the results of the linear theory is presented in § 3, followed by a brief description of the weakly nonlinear theory that leads to the MS equation. Exact and numerical solutions of the MS equation are also reviewed in this section. In § 4 the numerical scheme used to address the full nonlinear model is first presented followed by results of simulations that investigate the effects of thermal expansion and external noise on the flame dynamics. Concluding remarks are made in the last section.

2. Hydrodynamic model

In the hydrodynamic theory, the flame of thickness l_f is assumed to be thin compared to the representative lengthscale L of the fluid flow. The characteristic flame thickness may be based, for example, on the thermal thickness $\mathscr{D}_{th}/S_L$ where $\mathscr{D}_{th}$ is the thermal diffusivity of the mixture and S_L the laminar flame speed. Viewed on the hydrodynamical scale, the flame zone is seen as a sheet separating fresh unburnt gas from burnt combustion products; see figure 2. The hydrodynamic model was derived systematically by Matalon & Matkowsky (1982) as a limit process expansion

for small $\delta = l_f/L$ (see also Matalon *et al.* 2003). Typically, premixed flames are nearly a millimetre thick, so that with L of the order of few centimetres, $\delta \lessapprox 0.1$. Since the Prandtl number Pr for commonly used combustible mixtures is of order unity, the Reynolds number $Re \equiv \rho_u S_L L/\mu = (\delta Pr)^{-1} \gg 1$. The flow field on either side is, therefore, determined by solving the incompressible Euler equations with different densities, ρ_b for the burnt and ρ_u for the unburnt gases respectively, with small $O(\delta)$ viscous corrections. Across the flame sheet the Rankine–Hugoniot relations, with $O(\delta)$ correction terms describing the influences of the diffusion processes occurring within the thin but finite flame zone, must be satisfied. Similarly, the flame speed relation contains $O(\delta)$ terms accounting for variations in flame curvature and hydrodynamic strain. In this work we consider a slightly simpler model associated with Markstein (1964), which retains the dependence of flame speed on flame curvature only, and uses the Rankine–Hugoniot relations without modification. Accounting for stretch effects and incorporating the $O(\delta)$ corrections in the jump relationships requires a non-trivial generalization of the numerical scheme that will be addressed in future studies.

The mathematical formulation consists of solving the Euler equations

$$\nabla \cdot \boldsymbol{v} = 0, \tag{2.1}$$

$$\rho \frac{\partial \boldsymbol{v}}{\partial t} + \rho(\boldsymbol{v} \cdot \nabla)\boldsymbol{v} = -\nabla p, \tag{2.2}$$

where $\boldsymbol{v}$ is the velocity field and p is the (small) deviation of the pressure from its ambient value. The density is a piecewise constant function, given by

$$\rho = \begin{cases} \rho_u & \text{(unburnt gas)} \\ \rho_b & \text{(burnt gas).} \end{cases} \tag{2.3}$$

Let the flame sheet be described by the function $\psi(\boldsymbol{x}, t) = 0$ with the convention that the unit normal $\boldsymbol{n} = \nabla\psi/|\nabla\psi|$ is directed towards the burnt gas, so that $V_f = -\psi_t/|\nabla\psi|$ is the propagation speed (in a fixed coordinate system) back along the normal. The Rankine-Hugoniot relations are

$$\left.\begin{aligned} [\![\rho(\boldsymbol{v}\cdot\boldsymbol{n} - V_f)]\!] &= 0, \\ [\![\boldsymbol{n} \times (\boldsymbol{v} \times \boldsymbol{n})]\!] &= 0, \\ [\![p + \rho(\boldsymbol{v}\cdot n)(\boldsymbol{v}\cdot\boldsymbol{n} - V_f)]\!] &= 0, \end{aligned}\right\} \tag{2.4}$$

where the bracket operator $[\![\ ]\!]$ defines the jump in the quantity across the flame sheet. The flame speed S_f defined as the normal velocity of the unburnt gas relative to the flame front, namely $S_f \equiv \boldsymbol{v}^* \cdot \boldsymbol{n} - V_f$ where $\boldsymbol{v}^* = \boldsymbol{v}(\psi = 0^-)$, satisfies the relation

$$S_f = S_L(1 - \mathscr{L}\kappa), \tag{2.5}$$

where $\kappa = -\nabla \cdot \boldsymbol{n}$ is the mean curvature and the coefficient $\mathscr{L}$ is the Markstein length. Being associated with effects resulting from the internal flame structure, $\mathscr{L}$ is of the order of the flame thickness l_f. Although Markstein introduced this coefficient in a phenomenological way, the more rigorous asymptotic analysis provides an explicit expression for $\mathscr{L}$, exhibiting a dependence on the composition of the mixture and, in particular, on the equivalence ratio (Matalon *et al.* 2003). For hydrocarbon–air mixtures, for example, $\mathscr{L}$ is generally positive and decreases monotonically as the mixture varies from lean to rich conditions. The opposite is true for light fuels, such as hydrogen–air mixtures, where $\mathscr{L}$ is found to decrease as the mixture varies from rich to lean conditions and may be even negative in sufficiently lean mixtures.

3. Linear and weakly nonlinear analysis

A plane deflagration wave, propagating into a quiescent mixture at a constant speed S_L, is a simple solution of equations (2.1)–(2.5). The velocity and pressure across the front, located at $y=-S_L t$ and separating the fresh mixture from the hot combustion products, are piecewise constants given by

$$v=\begin{cases}0, & \\ (\sigma-1)S_L, & \end{cases} \qquad p=\begin{cases}0, & y<-S_L t,\\ -(\sigma-1)\rho_u S_L^2, & y>-S_L t,\end{cases} \tag{3.1}$$

where $\sigma=\rho_u/\rho_b>1$ is the thermal expansion coefficient. For a typical $\sigma=6$, the velocity increases fivefold as the gas expands and there is a drop in pressure which, when compared to the ambient pressure, constitutes a small change of the order of the square of the Mach number. A linear stability analysis of the planar solution (Markstein 1964) yields the dispersion relation

$$(\sigma+1)\,\omega^2+2\,(1+\mathscr{L}k)\,\sigma k S_L\omega-(\sigma-1-2\mathscr{L}\sigma k)\,\sigma k^2 S_L^2=0 \tag{3.2}$$

for the growth rate ω of a disturbance of wavenumber k. This relation reduces to the Darrieus–Landau result when $\mathscr{L}=0$, in which case

$$\omega=\omega_{DL}S_L k, \qquad \omega_{DL}\equiv\frac{-\sigma+\sqrt{\sigma^3+\sigma^2-\sigma}}{\sigma+1},$$

so that perturbations of all wavelengths grow and the instability increases indefinitely with increasing wavenumber. The hydrodynamic instability results from the gas expansion and the growth rate increases with increasing σ and vanishes as $\sigma\to 1$. When $\mathscr{L}\neq 0$, the growth rate is given by

$$\omega=\left\{-\frac{\sigma\,(1+\mathscr{L}k)}{\sigma+1}+\frac{1}{\sigma+1}\sqrt{\sigma^3+\sigma^2-\sigma+(\mathscr{L}k-2\sigma)\,\mathscr{L}k\sigma^2}\right\}S_L k.$$

It can be easily verified that for $\mathscr{L}<0$ the plane flame remains unconditionally unstable with disturbances growing at a rate ω higher than ω_{DL}. In contrast, for $\mathscr{L}>0$ the model has stable and unstable ranges of wavenumber. Long-wavelength disturbances still grow while short-wavelength disturbances are stabilized. The stabilization mechanism is readily understood – the enhanced flame speed at the crests ($\kappa<0$) as viewed from the unburnt side, and similarly the reduced speed at the troughs, tend to reduce the amplitude of the corrugations and flatten out the perturbed flame. The critical wavenumber is given by $k_c=(\sigma-1)/2\mathscr{L}\sigma$ and the corresponding wavelength is $\lambda_c=4\pi\mathscr{L}\sigma/(\sigma-1)$. Accordingly, disturbances with wavelength $\lambda<\lambda_c$ are stable and those with $\lambda>\lambda_c$ are unstable. The wavelength of the most amplified disturbance is determined by setting $\mathrm{d}\omega/\mathrm{d}k=0$.

The planar flame is unconditionally stable in a finite domain of width $L<\lambda_c$, because no linearly unstable mode of this solution fits in this domain. If L represents the characteristic transverse dimension it is convenient to introduce the scaled Markstein number

$$\alpha\equiv\mathscr{L}/(\sigma-1)L, \tag{3.3}$$

so that stability is ensured when $\alpha>(4\pi\sigma)^{-1}\equiv\alpha_c$. Note that $\alpha=O(\delta)$ and, since equation (3.2) is valid for $\delta\ll 1$, the dispersion relation may be written as

$$\omega\sim\omega_{DL}S_L k-\frac{\sigma\,(\sigma+\omega_{DL})}{\sigma+(\sigma+1)\,\omega_{DL}}\mathscr{L}S_L k^2\,.$$

This expression is similar in form to the dispersion relation obtained asymptotically using the more complete hydrodynamic model (Matalon & Matkowsky 1982; Pelce & Clavin 1982), except that the latter provides a more accurate expression for the $O(k^2)$ term and, in particular, relates the Markstein length $\mathscr{L}$ to fundamental physicochemical parameters, namely molecular and thermal diffusivities, overall activation energy and reaction orders of the chemical scheme, mixture equivalence ratio and burnt-to-unburnt density contrast. Viscous effects were found to play a secondary role in stability, which *a posteriori* justifies their being neglected in the analysis leading to (3.2).

Beyond the linear growth, when the unstable modes have grown to sufficiently large amplitudes, nonlinear effects may no longer be neglected. The complete reactive Navier–Stokes equations must then be solved numerically but, as noted in the Introduction, only a few such studies have been reported in the literature. Analytical insight may be achieved in the weakly nonlinear regime, by assuming that $\sigma - 1 \ll 1$. Since in this limit the Darrieus–Landau growth rate $\omega_{\mathrm{DL}} \sim (\sigma - 1)/2$ is relatively small, the evolution is described on the slow timescale $\tau = (\sigma - 1)t$ with the perturbed front expressed in the form

$$y = -S_{\mathrm{L}} t + (\sigma - 1)\phi, \qquad \phi = \phi(x, \tau). \tag{3.4}$$

We have restricted attention here to the two-dimensional case, but the extension to three dimensions is straightforward. If, for consistency, velocities and pressure are re-scaled as $\boldsymbol{v} = (\sigma - 1)^2 \tilde{\boldsymbol{v}}$ and $p = (\sigma - 1)^2 \tilde{p}$, the flame speed relation (2.5) yields

$$\phi_\tau + \frac{1}{2} S_{\mathrm{L}} \phi_x^2 - \frac{\mathscr{L} S_{\mathrm{L}}}{\sigma - 1} \phi_{xx} - \tilde{v}^* = o(\sigma - 1)^2 \tag{3.5}$$

where subscripts denote differentiation and $\tilde{v}^*$ is the axial velocity component evaluated at the unburnt side of the flame front. The reduced Euler equations, correct to $O(\sigma - 1)^2$, can be solved to give

$$\tilde{v}^* = \frac{1}{4\pi} \int_{-\infty}^{\infty} \int_{-\infty}^{\infty} |k| \, \mathrm{e}^{\mathrm{i}k(x-\xi)} \, \phi(\xi, \tau) \, \mathrm{d}k \, \mathrm{d}\xi \equiv \tfrac{1}{2} \mathrm{I}\{\phi\},$$

which when substituted into (3.5) yields a single nonlinear integro-differential equation for the determination of the flame displacement ϕ. Let L, the transverse domain of integration, be used as a unit of length, S_{L} as a unit of speed and L/S_{L} as a unit of time, the evolution equation in dimensionless form becomes

$$\phi_\tau + \tfrac{1}{2} \phi_x^2 - \alpha \phi_{xx} - \tfrac{1}{2} \mathrm{I}(\phi) = 0. \tag{3.6}$$

This equation is known as the Michelson–Sivashinsky (MS) equation after the authors who derived it and also provided the first numerical integration (Sivashinsky 1977; Michelson & Sivashinsky 1977). The operator $\mathrm{I}\{\phi\}$ is a linear, singular, non-local operator which constitutes a multiplication by $|k|$ in the Fourier space; i.e. $\mathrm{I}\{\cos(kx)\} = |k| \cos(kx)$. It may also be expressed as the Hilbert transform (denoted by $\mathscr{H}$) of the derivative of ϕ, namely $\mathrm{I}\{\phi; x\} = -\mathscr{H}\{\phi_x; x\}$.

On the finite domain $0 \leqslant x \leqslant 1$ with periodic boundary conditions, the MS equation admits exact solutions of the form

$$\phi = -U\tau + \Phi(x), \tag{3.7}$$

which correspond to steadily propagating patterns, namely they propagate (in the direction $\phi < 0$) at a constant speed U without change in shape. Upon taking the

spatial average, the MS equation yields

$$U = \tfrac{1}{2}\left\langle \Phi_x^2 \right\rangle \equiv \tfrac{1}{2}\int_0^1 \Phi_x^2 \, \mathrm{d}x, \tag{3.8}$$

so that the fractional increase in propagation speed is equal to the fractional increase in surface area of the flame front. The solutions of the form (3.7) are obtained by a pole decomposition technique (Thual, Frish & Henon 1985; Vaynblat & Matalon 2000*a*, *b*), and of particular interest is the set of *coalescent pole solutions* for which all the poles, $z_n = x_c \pm \mathrm{i}y_n$, are aligned parallel to the imaginary axis with x_c the common real part. The members of this family are distinguished by the number of poles N (or more precisely the number N of pairs of complex-conjugate poles) that contribute to the solution, and take the form

$$\Phi_{_N}(x) = -2\alpha \sum_{n=1}^{N} \ln \tfrac{1}{2}[\cosh(y_n) - \cos(2\pi x - x_c)].$$

The imaginary parts of the poles, y_n, are the solutions of N nonlinear algebraic equations

$$\coth y_n + \sum_{l\neq n;\, l=1}^{N} \coth\left[\tfrac{1}{2}(y_n - y_l)\right] + \coth\left[\tfrac{1}{2}(y_n + y_l)\right] = \frac{1}{4\pi\alpha}, \qquad n = 1, \ldots, N.$$

Although simple expressions can be written for $N = 1$ and 2, the y_n for $N > 2$ are calculated numerically; see Vaynblat & Matalon (2000*a*). The pole solutions correspond to cusp-like structures, with the (common) real part of the poles x_c representing the location of the 'cusp' and the imaginary part representing its height. The flame front shown in figure 2 is a representative pole solution, extended periodically in x. The propagation speed for the N-pole solution is obtained from (3.8) as

$$U_{_N} = 2\pi N\alpha(1 - 4\pi N\alpha). \tag{3.9}$$

To discuss the properties of the pole solutions it is convenient to introduce the reciprocal of the Markstein number, $\gamma = (2\pi\alpha)^{-1}$, which is directly proportional to the transverse size of the domain of integration. For a given γ, there is an upper bound on the number of poles that a member of the family of coalescent pole solutions possesses, i.e. $N \leqslant N_0(\gamma)$. The trivial solution $\Phi = 0$, which may be considered as the zero-pole solution, exists for all $\gamma > 0$. At $\gamma = 2$ the one-pole solution emerges as a new bifurcating solution; at $\gamma = 6$ the two-pole solution branches out and, in general, the N-pole solution bifurcates from the $(N-1)$-pole solution at $\gamma = 2(2N-1)$. Of greatest importance are the stability results of Vaynblat & Matalon (2000*a*, *b*), which show that for any value of γ there exists one and only one asymptotically stable coalescent pole solution, and that the stable solution corresponds to the one with the maximum number of poles $N_0(\gamma)$. Accordingly, the planar flame front, or zero-pole solution, is the stable solution for $\gamma < 2$, the one-pole solution is the stable solution for $2 < \gamma < 6$, the two-pole solution is the stable solution for $6 < \gamma < 10$, etc .... As γ increases, the stable equilibrium states of the MS equation undergo a cascade of supercritical bifurcations corresponding to structures of deeper and deeper 'cusps' that propagate at a speed that increases with increasing γ and asymptotes to a constant value $U_\infty = 1/8$. As $\gamma \to \infty$ (or $\alpha \to 0$), the shape of the solution tends to a genuine cusp (of finite amplitude) that propagates at a speed U_∞. The dependence of the speed U on γ is shown in figure 8(*a*).

The stability properties discussed above imply that, for a given γ, the long-time behaviour of the solution of the MS equation, starting with arbitrary initial data,

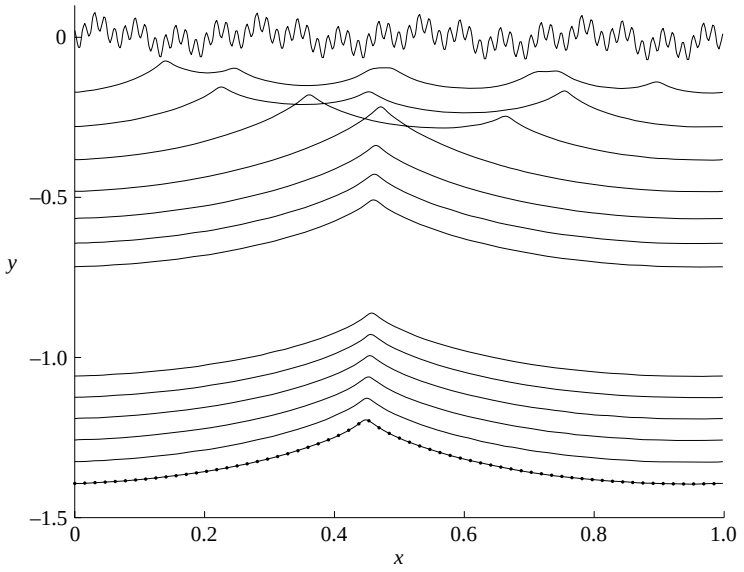

FIGURE 3. Development of the flame front profile $\phi(x, \tau)$, based on the MS equation for $\alpha = 0.005$, starting with arbitrary initial data. The small disturbances introduced through the initial conditions merge, forming bigger cells which eventually coalesce into a single-peak structure that coincides with the pole solution ($N = 8$), shown in the figure as the dotted curve.

would converge to the steady propagating N_0 -pole solution. In a typical numerical experiment, as illustrated in figure 3 for $\alpha = 0.005$, the short-wavelength corrugations introduced through initial disturbances merge, forming bigger cells as time progresses which eventually coalesce into a single-peak structure filling up the entire interval (see also Michelson & Sivashinsky 1977; Gutman & Sivashinsky 1990). The solution appears to converge to the corresponding pole solution ($N = 8$) illustrated in the figure by the dotted curve. Hence, for moderate values of γ the flame develops into a relatively large single-peak structure which, in dimensional form, has a wavelength comparable to L and amplitude proportional to $\sigma - 1$. The transverse dimension L is generally much larger than the wavelength corresponding to the most amplified small disturbance predicted by the linear theory. The cusp-like structure propagates in the negative y-direction at a constant speed without further change in shape.

The general structure of the solution is retained in computations carried out for large γ (small α) except that now small wrinkles appear repeatedly on the flame front, the speed of propagation varies continuously in time and the solution does not settle to a steadily propagating state. This is illustrated in figure 4 for $\alpha = 0.002$, computed with the same spatial resolution as figure 3. (The solution in both cases was computed using a spectral method; the numerical scheme is described below in § 4.3). Although the short-wavelength corrugations introduced through the initial disturbances merge to form a large single-peak structure, small-scale wrinkles keep appearing on the flame front, contaminating its surface. It has been tempting to associate this peculiar behaviour with a secondary instability that occurs at a critical value of α (Rahibe, Aubry & Sivashinsky 1998), but this was proven incorrect – the stability results of the pole solutions imply that a single-cusp structure in a finite domain L is unconditionally stable no matter how large L is. Therefore, the unsteady structure in the numerical simulation does not represent a self-sustained phenomenon, but rather

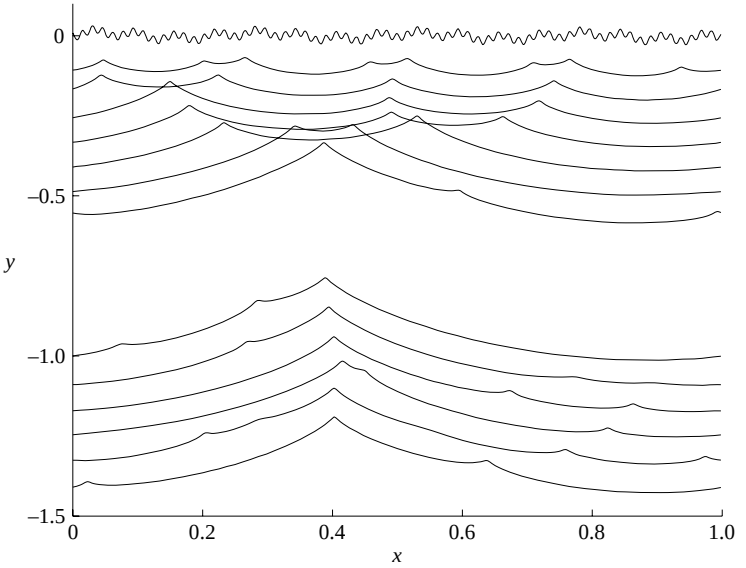

FIGURE 4. Development of the flame front profile $\phi(x, \tau)$, based on the MS equation for $\alpha = 0.002$, starting with arbitrary initial data. The small disturbances introduced through the initial conditions merge, forming bigger cells which eventually coalesce into a single-peak structure, but the solution never settles into a steady state as small-scale wrinkles keep appearing sporadically on the flame front.

an acute sensitivity to numerical noise, as suggested by Joulin (1989). The unsteady pebbly structure observed experimentally on the propagation fronts of sufficiently large flames (Strehlow 1984; Groff 1982; Bradley *et al.* 2001) are not entirely the product of initial disturbances but rather require some level of background noise which, when amplified by the hydrodynamic instability, acts to sustain the multi-scale nature of the flame front. The effect of noise will be further discussed below.

4. Fully nonlinear model – numerical simulations

We now address the full nonlinear problem in order to understand the effects of finite-amplitude disturbances and realistic values of thermal expansion σ on flame dynamics. We start with a brief discussion of the numerical approach used in solving the free-boundary problem (2.1)–(2.5).

4.1. *Numerical scheme*

The numerical scheme is based on a continuum approach where singular sources and discontinuities are smoothed properly over several computational grid cells. For the density, the distribution

$$\rho(\psi) = \rho_u + \tfrac{1}{2}(\rho_b - \rho_u)\left[1 + \tanh\frac{\psi}{h}\right] \tag{4.1}$$

centred at the flame front is chosen, with h the grid size. For a typical value of $\sigma = 6$, for example, the density reaches the constant values ρ_u and ρ_b to within 99% in a distance of four grid cells. The flame sheet $\psi(\boldsymbol{x}, t) = 0$ is now a level set of the density distribution function corresponding to $\rho = (\rho_u + \rho_b)/2$. Conservation of mass across the sheet is satisfied by introducing a source term to the divergence-free relation (2.1),

namely

$$\nabla \cdot \boldsymbol{v} = \rho_{\mathrm{u}} S_{\mathrm{f}} \frac{\partial}{\partial n}\left(\frac{1}{\rho}\right), \tag{4.2}$$

where $\partial/\partial n$ denotes the directional derivative along the normal to the sheet. A small viscous term is added to the momentum equation (2.2) in order to introduce a small degree of dissipation in the system. Thus

$$\rho \frac{\partial \boldsymbol{v}}{\partial t} + \rho(\boldsymbol{v} \cdot \nabla)v = -\nabla p + \mu \nabla^2 \boldsymbol{v}, \tag{4.3}$$

where μ is the viscosity of the mixture. In the calculations reported below we have taken a large Reynolds number, $Re = 10^5$, to effectively simulate an inviscid flow, and verified that no significant change occurs when it is increased to $Re = 10^6$. It is easy to see that, when $h \to 0$, the density distribution (4.1) approaches the piecewise-constant function (2.3), and equations (4.2)–(4.3) reduce to (2.1)–(2.2) with the jump relations (2.4) automatically satisfied. Finally, the propagation law (2.5) yields an evolution equation

$$\psi_t + \boldsymbol{v}^* \cdot \nabla \psi = S_{\mathrm{f}} |\nabla \psi| \tag{4.4}$$

for the shape and location of the flame sheet $\psi(\boldsymbol{x}, t) = 0$, where

$$S_{\mathrm{f}} = S_{\mathrm{L}} [1 + \mathscr{L} \nabla \cdot (\nabla \psi / |\nabla \psi|)]. \tag{4.5}$$

Equations (4.2)–(4.3) were solved using the variable-density IAMR code developed at the Lawrence Berkeley National Laboratory for solving the incompressible Navier–Stokes equations of a variable-density flow modified appropriately for the additional source terms. The algorithm in this code uses a fractional step approach, with second-order upwind Godunov methodology for the advection step, Crank–Nicolson discretization of the viscous and diffusive terms, and a variable-density approximate second-order projection to impose the divergence constraint (Almgren, Bell & Szymczak 1996). A level-set method is used as a front-capturing technique, with the propagation velocity extension algorithm proposed by Sethian (1996). In order to stabilize the scheme, upwind and central difference schemes are used for the convective and diffusive terms, respectively. Note that in solving (4.4) it is necessary to evaluate $\boldsymbol{v}^*$ on the Langragian mesh representing the flame surface and this is accomplished in the spirit of the immersed boundary method of Peskin (1977). Further details about each of these steps can be found in Rastigejev & Matalon (2006).

4.2. *Effect of thermal expansion*

Most of the results presented below are based on simulations carried out on a computational domain $[0, 1] \times [0, 2]$, using 256 points/unit length, with periodic boundary conditions applied to the sidewalls. For large values of α a coarser grid was sufficient to ensure high enough accuracy.

To establish the accuracy of the numerical scheme, we first consider $\sigma = 1.1$ and compare the flame shape of the steady state, obtained as the long-time behaviour of the computed solution, with the corresponding profile of the exact pole solution $\Phi_N(x)$. The results are illustrated in figure 5 for the two values $\alpha = 0.02$ and 0.007, corresponding to $N = 2$ and $N = 6$ respectively, with the numerical simulations represented by solid curves and the analytical pole solutions by dotted curves. For proper comparison, the computed flame shape profile has been re-scaled with respect to $\sigma - 1$ (see (3.4)). A very good agreement exists for $\alpha = 0.02$, as expected. For the smaller value of α the agreement is quite good and could have been improved if the

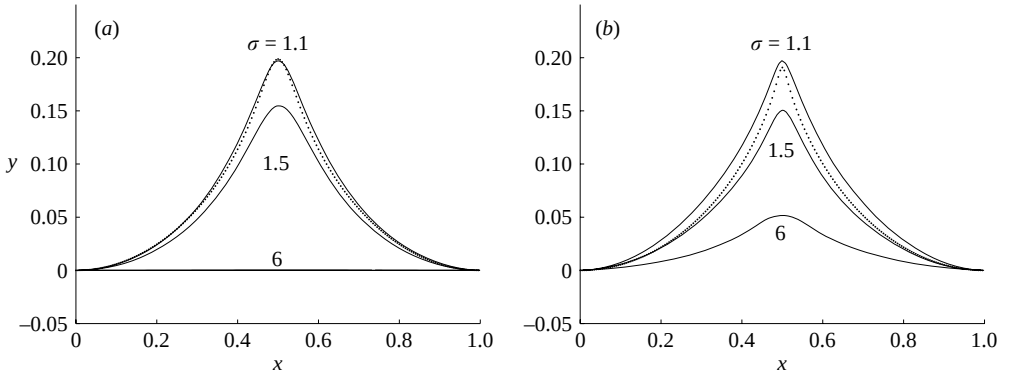

FIGURE 5. Comparison between the steady-state solutions computed based on the full nonlinear model (solid curves) and the exact pole solutions of the MS equation (dotted curve), for several values of σ with (*a*) $\alpha = 0.02$, (*b*) $\alpha = 0.007$.

simulation had been carried out on a finer grid. The figure also shows flame profiles for two other values of thermal expansion. For $\sigma = 1.5$ the computed results are quantitatively close to the pole solutions even though the 'small parameter' $\sigma - 1 = 0.5$. For $\sigma = 6$, however, the results are markedly different and will be discussed below.

We now turn attention to more realistic values of the thermal expansion and choose $\sigma = 6$ for illustrative purpose. The time evolution of an initial cosine perturbation is shown in figure 6 for the three values $\alpha = 0.005, 0.0025, 0.001$. The flame front profile is plotted for consecutive times, starting from the top figure, over the time intervals specified in the figure caption. For consistency the scaled time τ has been used as reference. For $\alpha = 0.005$ a smooth cusp-like structure develops early on and propagates at a constant speed without further change in shape. A similar behaviour occurs when $\alpha = 0.0025$, but the transient behaviour in this case extends over a slightly longer time and a smooth structure develops only at $\tau \approx 12$–14. For $\alpha = 0.001$ the flame profile does not seem to converge to a smooth surface, even after a sufficiently long time ($0 \leqslant \tau < 15$). Although the overall shape is similar to the single-peak structure observed for the larger values of α, the flame does not reach a steady state. Even when it appears that a single-peak structure has developed (for $\tau \approx 13$, for example), small wrinkles develop sporadically on the flame front as it propagates further, contaminating its surface. This becomes more evident in figure 7, where a smaller value of $\alpha = 0.0005$ was selected. It is interesting to note that, as α decreases, the cusp appears sharper and sharper and the 'parabolic' convex part of the flame gets flatter, as predicted by the exact pole solutions. A closer examination of the result indicates that the wrinkles appear first on the troughs, where the curvature is relatively weak, and propagate along the surface towards the crest where they are annihilated.

We have just seen that for values of α that are not too small, the flame profile settles to a steady state. The long-time behaviour of the solution for $\alpha = 0.02$ and 0.007 is shown in figure 5 for $\sigma = 6$. For $\alpha = 0.02$ the flame regains its planar shape since $\alpha > \alpha_c \approx 0.0133$. But for $\alpha = 0.007$ a cusp-like structure does emerge as expected. It should be noted that, when comparing with the profiles for the smaller values of σ, the graph must be amplified by the factor $\sigma - 1$. For realistic values of σ the solution has, therefore, a significantly larger amplitude: $\Phi_{\max} \approx 0.25$ for $\sigma = 6$ compared to the value 0.2 predicted by the pole solution.

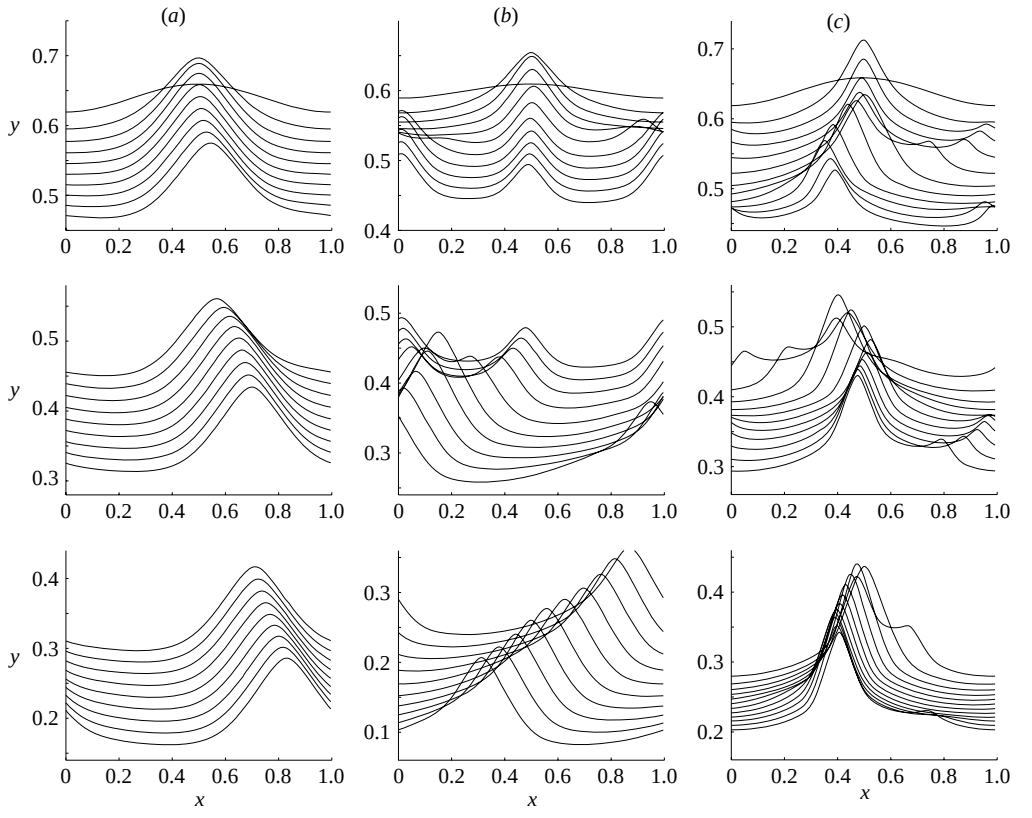

FIGURE 6. The time evolution of an initial cosine perturbation for the three values: (*a*) $\alpha = 0.005$, (*b*) $\alpha = 0.0025$ and (*c*) $\alpha = 0.001$ with $\sigma = 6$. The (scaled) flame profiles are plotted at consecutive times (top to bottom) over the intervals: (*a*) $\tau \in (0, 18)$, (*b*) $\tau \in (0, 20)$ and (*c*) $\tau \in (0, 15)$.

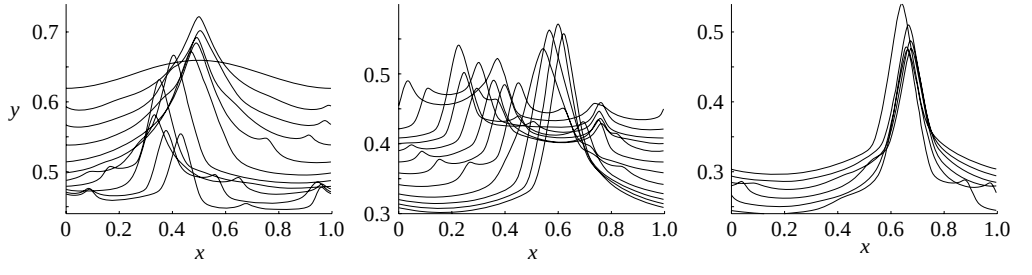

FIGURE 7. The time evolution of an initial cosine perturbation for $\alpha = 0.0005$ with $\sigma = 6$. The (scaled) flame profiles are plotted for consecutive times (left to right) over the interval $\tau \in (0, 10)$.

The small-scale unsteady behaviour uncovered for small α is similar to what has been observed in numerical simulation of the MS equation, except that for the more realistic values of σ just presented the first appearance of the small-scale wrinkles on the surface of the flame front (for a given grid resolution) occurs at a much smaller value of α. This unsteady behaviour is apparently associated with the amplification

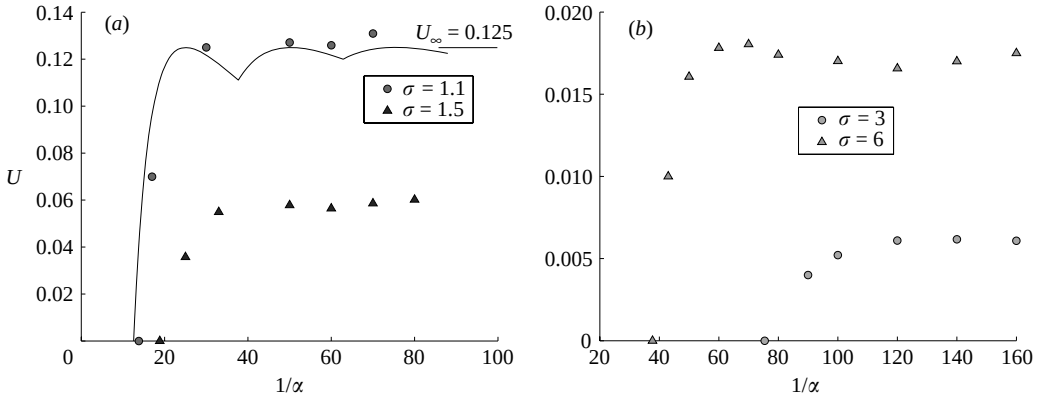

FIGURE 8. The (scaled) incremental increase in propagation speed U as a function of $1/\alpha$. The results in (a) are plotted for values of σ near one, and are compared to the the exact pole solution of the MS equation (solid curve). The results in (b) are plotted for $\sigma = 3$ and 6. Note that in dimensional form the speed is amplified by a factor $(\sigma - 1)^2$.

of background noise coupled to the hydrodynamic instability, an assertion that will be further discussed below.

As noted earlier, a planar propagating flame loses stability at $1/\alpha_c = 4\pi\sigma$ giving rise to a steadily propagating cusp-like structure. The incremental increase in propagation speed of the corrugated front for $1/\alpha > 1/\alpha_c$ is shown in figure 8 for several values of σ. The ordinate in this figure represents the scaled increment in speed U, which in dimensional form is given by

$$\hat{U} = (\sigma - 1)^2 U S_L,$$

so that the corrugated front propagates as a whole in the negative y-direction with a speed $S_L + \hat{U}$. Figure 8(a) corresponds to values of σ sufficiently close to one and allows a comparison with the exact pole solution of the MS equation represented by the solid curve. For $\sigma = 1.1$ the results of the numerical simulations are in very close agreement with the exact solution. The incremental change in speed increases with increasing $1/\alpha$ and tends asymptotically to $U_\infty = 0.125$. A similar behaviour is seen for $\sigma = 1.5$; the incremental speed here tends asymptotically to $U_\infty \approx 0.06$. Figure 8(b) shows the results of the numerical simulations for $\sigma = 3$ and 6. They are qualitatively similar to those predicted by the MS model, with U increasing from zero at the bifurcation point $1/\alpha_c$ (which increases with increasing σ) tending respectively to $U_\infty \approx 0.0165$ and 0.006 as $1/\alpha \to \infty$. This amounts to an increase in speed of 7–15% for the two cases presented.

Figure 9 shows the dependence of the incremental increase in propagation speed on thermal expansion for a given Markstein number $\mathscr{L}/L$. Two separate graphs are shown for two separate range of σ. Results are only presented for values of α that yield steadily propagating structures, namely values of α that are not too small (see also the discussion in the next section). Consequently, the smaller the range of $\sigma - 1$, the smaller the lower bound on $\mathscr{L}/L$. The dependence of the propagation speed on thermal expansion appears nearly linear. This result is consistent with the prediction (3.9) of the MS equation which, when expressed in dimensional form and use is made of the definition (3.3) of α, shows that the propagation speed is a piecewise-linear function of σ. The dependence on thermal expansion also appears independent of small changes in the Markstein number. Indeed, as shown in figure 8, except for near

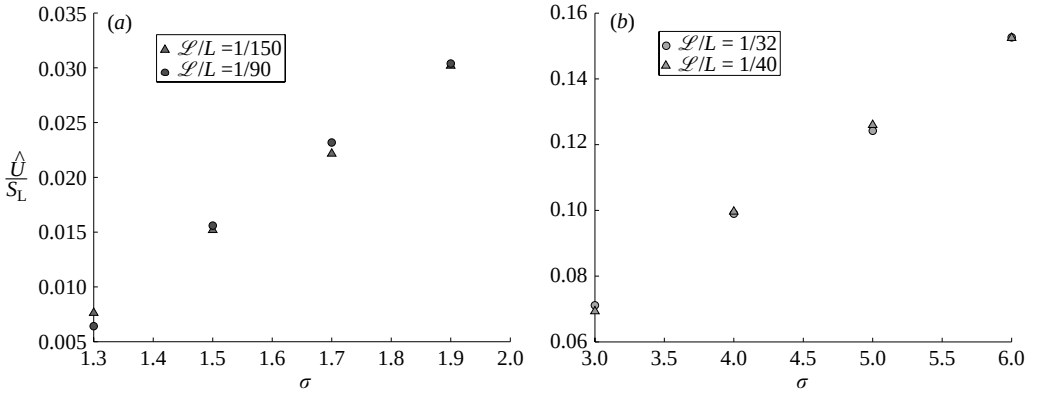

FIGURE 9. The dependence of the incremental increase in propagation speed $\hat{U}/S_L$ on thermal expansion, for given values of the Markstein number $\mathscr{L}/L$.

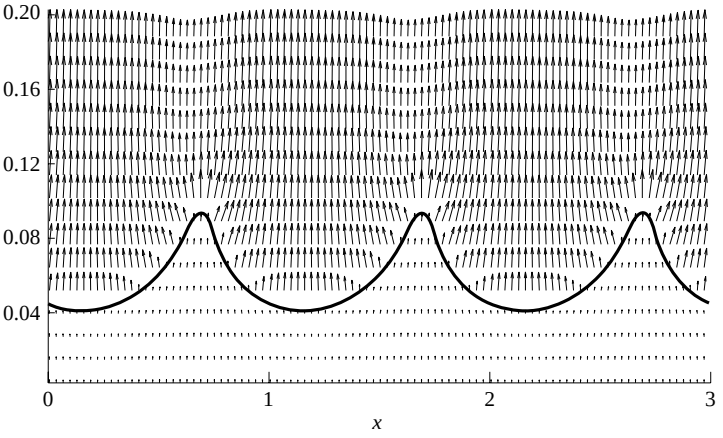

FIGURE 10. Flow field, depicted by velocity vectors, across a corrugated flame front represented by the solid curve; calculated for $\sigma = 6$ and $\alpha = 0.007$.

the bifurcation point $1/\alpha_c$, the propagation speed U reaches a plateau and remains nearly independent of further changes in α.

Although the emphasis in this work has been on the evolution of the flame front, our computations also provide accurate information about the flow field, as illustrated in figure 10. The velocity vectors in the figure clearly show the deflection of the streamlines upon crossing the flame front, and that the flow remains uniform far upstream and far downstream, as it should.

4.3. *Effect of external noise*

In order to investigate the effect of external noise on flame dynamics consistently, the amount of numerical noise must be reduced significantly so as not to affect the dynamics of the propagating flame. The calculations must be therefore performed on a very fine mesh. As shown below, even for relatively large values of α, when the flame front becomes sensitive to external noise, a grid of as many as 8000 points is needed to prevent the wrinkling of the flame interface. Because of limitations in computational resources this resolution cannot be achieved in the two-dimensional simulations based on the full nonlinear model. Our investigation will therefore be

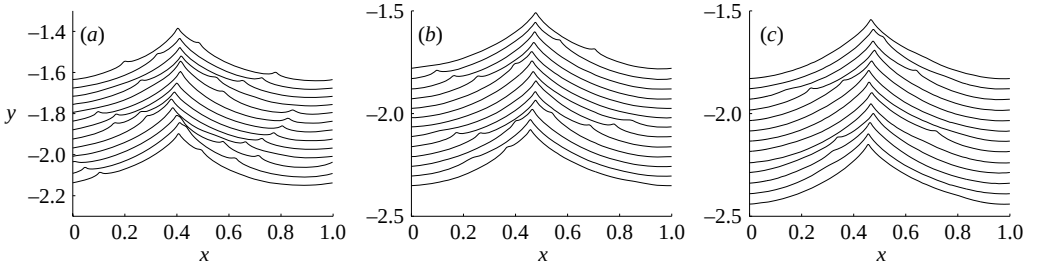

FIGURE 11. Flame profiles computed based on the MS equation for $\alpha = 0.002$ with (*a*) $N = 512$, (*b*) $N = 2048$ and (*c*) $N = 8192$ Fourier modes for consecutive times with time intervals $\Delta\tau = 0.04$.

carried out within the context of the one-dimensional simplified MS model which, as already noted, exhibits qualitatively the same phenomenon.

The MS equation (3.6) has been solved numerically using a Galerkin method. The function $\phi(x)$ on $0 < x \leqslant 1$ is represented at the uniformly distributed collocation points $x_n = n/N$, where $n = 1, \ldots, N$, by the Fourier truncated series

$$\phi(x_n, \tau) = \sum_{k=-N/2+1}^{N/2} a_k(\tau)\, \mathrm{e}^{2\pi \mathrm{i} nk/N},$$

with coefficients

$$a_k(\tau) = \frac{1}{N} \sum_{n=-N/2+1}^{N/2} \phi_n \mathrm{e}^{-2\pi \mathrm{i} nk/N} \equiv \mathscr{P}_k[\phi], \quad \phi_n \equiv \phi(x_n, \tau).$$

Substituting into equation (3.6) yields

$$\frac{\mathrm{d}a_k}{\mathrm{d}\tau} + \tfrac{1}{2} P_k[(\mathscr{D}\phi)^2] + 4\pi^2 k^2 a_k - \pi|k| a_k = 0, \qquad k = -N/2+1, \ldots, N/2,$$

where

$$\mathscr{D}\phi = 2\pi \mathrm{i} \sum_{k=-N/2+1}^{N/2} a_k(\tau) k\, \mathrm{e}^{2\pi \mathrm{i} nk/N}$$

is the approximation of ϕ_x. When solving these equations, the linear and nonlinear terms were discretized respectively with Crank–Nicolson and Adams–Bashforth approximations, resulting in a second-order-accurate scheme (in time). In the calculations presented below a time step $\Delta\tau = 10^{-5}$ was used.

Numerical experimentation has been carried out to investigate the dynamics of the small-scale wrinkles that were seen to appear sporadically on the flame surface for small values of α. The appearance of wrinkles was found to be highly sensitive to the level of numerical noise, which is reduced by increasing the number of Fourier modes used in the Galerkin approximation. This is illustrated in figure 11 showing flame profiles calculated for $\alpha = 0.002$, corresponding to a 20-pole solution, with three different grid resolutions. Three to four wrinkles are present at any time when 512 Fourier modes are used, but only one to two wrinkles are present when 2048 Fourier modes are used. With $N = 8192$ Fourier modes, there are very few wrinkles during the entire time interval shown in the figure and, although they seem to disappear towards the end of this time interval, new wrinkles will reappear if one waits long enough.

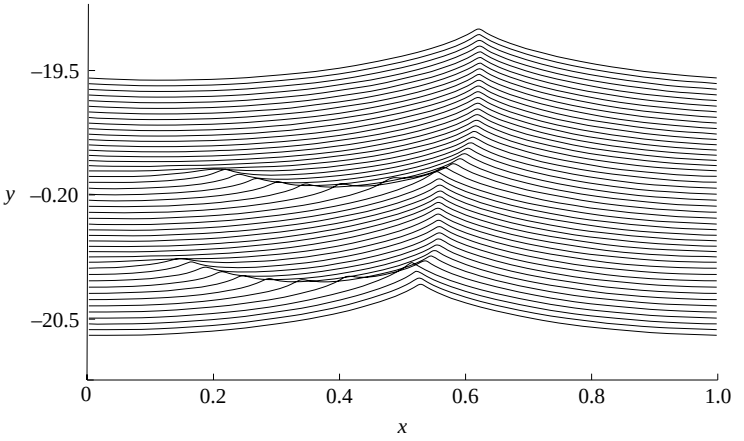

FIGURE 12. Flame profiles computed based on the MS model for $\alpha = 0.004$ with $N = 512$ Fourier modes. The profiles are shown for consecutive times with time intervals $\Delta\tau = 0.178$.

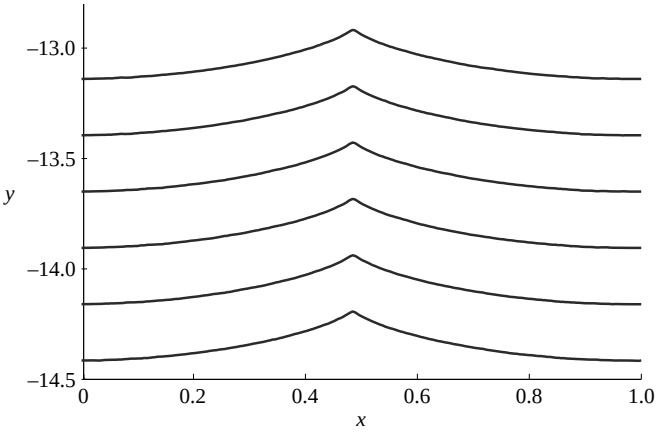

FIGURE 13. Flame profiles computed based on the MS model for $\alpha = 0.004$ with $N = 8192$ Fourier modes. The profiles are shown for consecutive times with time intervals $\Delta\tau = 2$.

The number of wrinkles retained on the flame surface during a given time interval is, therefore, sensitive to the level of numerical noise.

Next, we present three sets of numerical simulations with a somewhat larger $\alpha = 0.004$, corresponding to a 10-pole solution. For the first simulation a relatively low number of Fourier modes $N_1 = 512$ was used. Wrinkles begin to appear in this case at approximately $\tau = 50$. In figure 12 flame profiles are shown at consecutive time intervals with $\Delta\tau = 0.178$, within the time period $\tau = 156$–164. As in previous numerical simulations, the wrinkles originate at the troughs and propagate along the flame surface towards the crest where they eventually disappear.

For the second simulation, a large number of Fourier modes $N_2 = 8192$ was selected. The integration was carried out up to time $\tau = 1000$, which is approximately 20 times larger than in the previous numerical experiment, and no wrinkles were ever observed. The solution shown in figure 13 rapidly stabilizes to a steady state that coincides with the 10-pole solution, as it should, and continues to propagate with a constant

speed, without changing shape. The profiles in this figure are shown at consecutive time interval with $\Delta\tau = 2$, within the time period $\tau = 990$–1000. Note that the flame dynamics for $\alpha = 0.004$ is less sensitive to numerical noise than the flame dynamics for $\alpha = 0.002$ shown in figure 11. Next, we performed a simulation with the same number of Fourier modes $N_2 = 8192$ as before, after having nullified the coefficients in the Fourier decomposition corresponding to the higher $N_{\text{high}} = 8192 - 512 = 7680$ frequencies, thus using only the low $N_{\text{low}} = 512$ frequencies. The spatial resolution achieved here is the same as for the first simulation, since the number of non-zero coefficients N_{low} is equal to the total number of Fourier modes N_1. However, unlike the first set of calculations, the so-called aliasing effect, where the solution is contaminated by high-frequency modes which appear on the discrete grid and cannot be properly distinguished from the correct low modes, is much lower in this case. One finds that no wrinkles are developed even when the integration is carried out over a sufficiently long time $\tau \sim 1000$, which is nearly 20 times as long as the time used in the first simulation shown in figure 12. Despite the much lower number of Fourier modes, the flame profiles are identical to those shown in figure 13 and will not be redrawn again. This suggests that the numerical noise associated with aliasing is indeed responsible for the generation of the small-scale wrinkles that develop on the flame surface.

The last numerical experiment is performed again with $N_2 = 8192$, but a low-amplitude external forcing term $\eta(x_n, \tau)$ representing noise has been added to the system. In Fourier space

$$\eta(x_n, \tau) = \sum_{k=-N/2+1}^{N/2} b_k(\tau)\, \mathrm{e}^{2\pi \mathrm{i}\, nk/N}$$

with the Fourier coefficients assuming the form $b_k = r_k(\tau)\mathscr{P}_k[f]$, where r_k is a randomly generated factor that take values in the interval $-0.5 < r_k < 0.5$ with equal probability, and $f(x - x_0)$ is a distribution function centred around some arbitrary x_0. In the present test we assumed a Gaussian distribution $f = A\exp[-\beta(x - x_0)^2]$ with $A = 2 \times 10^{-8}$, $\beta = 50$ and chose $x_0 = 0.2$. The noise has been introduced in the system by adding the random b_k to the Fourier coefficients a_k. The results are shown in figure 14(a) where flame profiles at consecutive time intervals $\Delta\tau = 0.3$ are plotted during the time period $\tau = 1.5$–10.5. The results clearly show the sporadic appearance of small-scale wrinkles that closely resemble those generated by numerical noise. The amplitude of the noise as a function of time is also shown in figure 14(b–d) at three sample points $x = 0.25$, 0.5, and 0.75.

The inclusion of noise mimics to some degree the influence of background physical noise that may result from small velocity fluctuations in the incoming flow far upstream. It is of interest, therefore, to examine its effect on the propagation speed. To this end, it is sufficient to consider a relatively large α, for which a steady state can be reached, and perform calculations on a relatively crude grid. For the results presented in figure 15 we chose $\alpha = 0.005$ and used a level-set method with $N = 256$ grid points. Figure 15(a) illustrates the dependence of the average propagation speed, defined as in equation (3.8), on time. In the absence of noise, the flame stabilizes to a steady state (corresponding to an 8-pole solution), and propagates thereafter at a constant speed, with $U \approx 0.124$ shown in the figure as a straight solid line. The propagation speed when noise is present varies non-uniformly in time as shown in figure 15(a). The appearance of wrinkles causes the flame to accelerate, with the propagation speed increasing further until the wrinkles merge at the crest. The

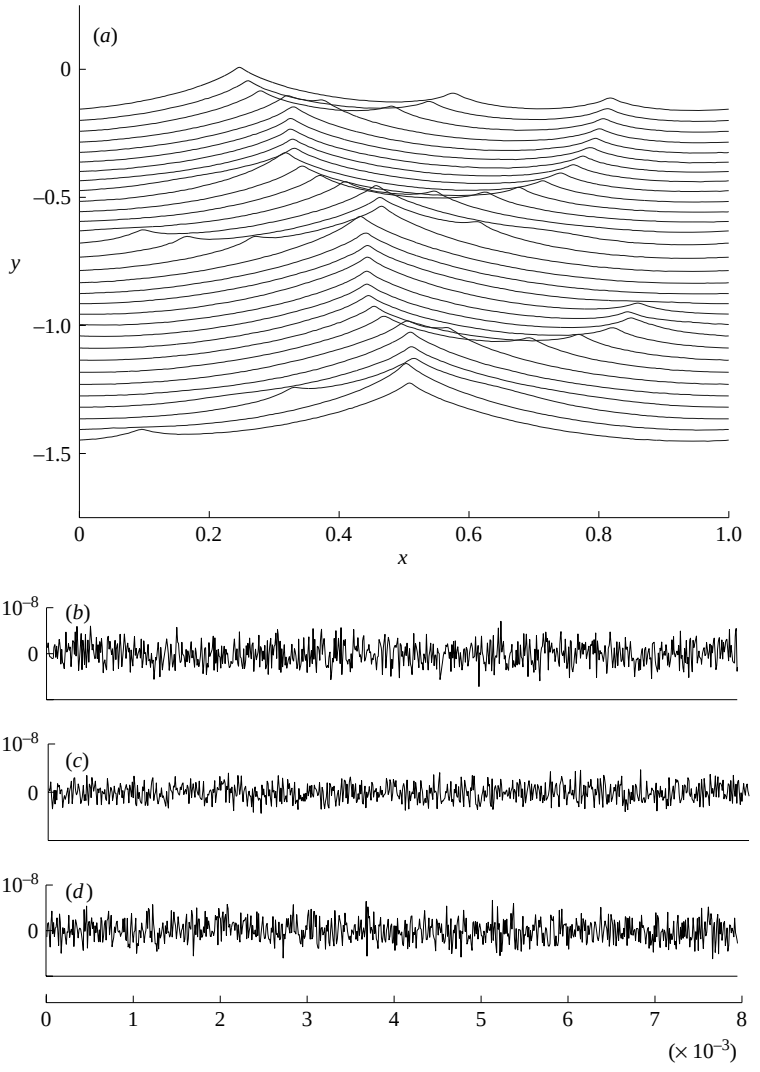

FIGURE 14. (*a*) Time evolution of a propagating flame subjected to external random noise calculated based on the MS equation with $\alpha = 0.005$. A sample of the noise (amplitude vs. time) introduced at the three sample locations: (*a*) $x = 0.25$, (*b*) $x = 0.5$ and (*c*) $x = 0.75$ is also shown in the figure.

disappearance of the wrinkles is associated with a drop in propagation speed, with the decrease in speed continuing either until the flame stabilizes to the appropriate pole solution, or until new wrinkles appear. This development is illustrated in figure 15(*b–e*). Flame profiles are shown during a short time interval near the times marked by (*b–e*) in (*a*). The times when the maximum speed is reached (marked *b* and *c*) correspond to the moments when the pair of wrinkles merge at the crest and disappear, while the times when the minimum speed is reached (marked by *d* and *e*) correspond to the moments when a new pair of wrinkles reappears on the flame surface. Finally, we note that on the average, the propagation speed is significantly increased (nearly doubled) in the presence of noise.

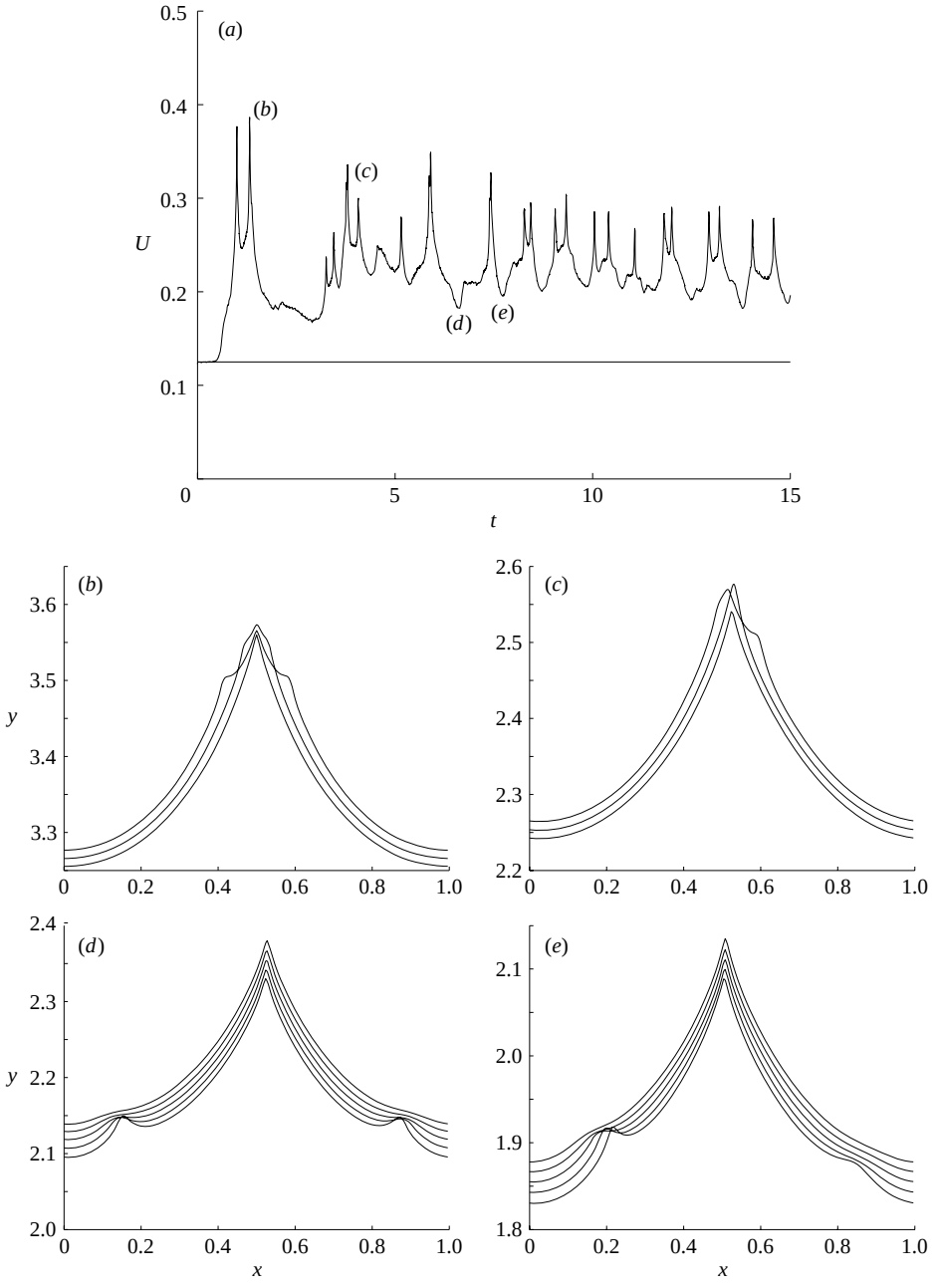

FIGURE 15. The (*a*) incremental increase in propagation speed of a corrugated flame subjected to noise, as a function of time. (*b–e*) The flame front profiles during the short time interval near the times marked by (*b–e*) in (*a*).

5. Conclusions

The nonlinear evolution of a perturbed premixed flame under the influence of the hydrodynamic instability has been discussed within the context of the Michelson–Sivashinsky equation for weak thermal expansion, $\sigma - 1 \ll 1$, and within the context

of a fully nonlinear hydrodynamic model for realistic values of thermal expansion, $\sigma - 1 = O(1)$. It was shown that the short-wavelength disturbances introduced through the initial conditions tend to merge, forming bigger corrugations which eventually coalesce into a single-peak structure (a cell) of transverse dimension L. The resulting cell size L is significantly larger than the wavelength of the most amplified disturbance predicted by the linear theory, and is determined by the overall dimension of the system. The flame shape, therefore, takes the form of wide and relatively flat troughs separated by narrow sharp crests that closely resemble the surface of experimentally observed flames. When the transverse dimension L is not too large, these structures are stable and propagate as a whole at a constant speed, larger than the speed of a planar flame. The propagation speed first increases as the Markstein number increases, but it quickly reaches an asymptote so that the relative increment in speed becomes independent of the mixtures's composition and of the lateral size. The dependence of propagation speed on thermal expansion is nearly linear.

When the transverse dimension L is large, the flame dynamics becomes sensitive to external noise. A low level of permanent noise provides small disturbances which are rapidly magnified by the hydrodynamic instability, resulting in small-scale wrinkles that appear sporadically on the flame, propagate along its surface, and disappear at the crests. A significant increase in overall speed associated with this complex, multi-scale structure results. This may explain the experimentally observed unsteady pebble-like structures on the propagation fronts of sufficiently large flames and the associated large increase in propagation speed. External noise may result, for example, from a weakly turbulent flow. If the turbulence scale is relatively large, the flow does not affect the internal flame structure and the flame may be viewed as a surface of density discontinuity, well within the realm of the present model. The turbulence provides a permanent level of noise that enables the sustaining of the multi-scale nature of the flame surface. This conjecture clearly requires a more detailed investigation; the numerical algorithm should be adjusted by introducing stochastic sources into the governing equations that more closely mimic 'physical noise,' and the numerical procedure should ensure that the energy associated with the simulated noise remains larger than the energy associated with the numerical noise.

This work has been partially supported by the National Science Foundation under grants DMS-0405129 and CTS-0074320.

REFERENCES

Almgren, A. S., Bell, J. B. & Szymczak, W. G. 1996 A numerical method for the incompressible Navier–Stokes equations based on an approximate projection. *SIAM J. Sci. Comput.* **17**, 358–369.

Bradley, D. 1999 Instabilities and flame speed in large-scale premixed gaseous explosions. *Phil. Trans. R. Soc. Lond.* A **357**, 3567–3581.

Bradley, D., Cresswell, T. M. & Puttock, J. S. 2001 Flame acceleration due to flame-induced instabilities in large-scale explosions. *Combust. Flame* **124**, 551–559.

Bychkov, V. V. 1998 Nonlinear equation for a curved stationary flame and the flame velocity. *Phys. Fluids* **10**, 2091–2098.

Darrieus, G. 1938 Propagation d'un front de flamme. Unpublished work, presented at La Technique Moderne (Paris), and in 1945 at Congrès de Mécanique Appliquée (Paris).

Denet, B. & Haldenwang, P. 1995 A numerical study of premixed flames Darrieus-Landau instability. *Combust. Sci. Technol.* **104**, 143–167.

Fox, M. D. & Weinberg, F. J. 1962 Experimental study of burner-stabilized turbulent flames in premixed reactants. *Proc. R. Soc. Lond.* A **268**, 222.

Groff, E. G. 1982 The cellular nature of confined spherical propane-air flames. *Combust. Flame* **48**, 51.

Gutman, S. & Sivashinsky, G. I. 1990 The cellular nature of hydrodynamic flame instability. *Physica* D **43**, 129–139.

Istratov, A. G. & Librovich, V. B. 1969 On stability of gasdynamic discontinuities associated with chemical reactions. Case of a spherical flame. *Acta Astronautica* **14**, 453–466.

Ivashchenko, P. F. & Rumyantsev, V. S. 1978 Convective rise and propagation velocity of a large flame focus. *Combust. Explosion Shock Waves* **14**, 338–341.

Joulin, G. 1989 On the hydrodynamic stability of curved premixed flames. *J. Phys. Paris* **50**, 1069–1082.

Kadowaki, S. 1999 The influence of hydrodynamic instability on the structure of cellular flames. *Phys. Fluids* **11**, 3426–3433.

Kazakov, K. A. & Liberman, M. A. 2002 Nonlinear equation for curved stationary flames. *Phys. Fluids* **14**, 1166–1181.

Landau, L. D. 1944 On the theory of slow combustion. *Acta Physicochimica USSR* **19**, 77–85.

Lind, C. D. & Whitson, J. 1977 Explosion hazards asssociated with spills of large quantities of hazardous materials. *Phase III Report No.* CG-D-85-77, *Department of Transportation, US Coast Guard Final Report*, ADA 047585.

Markstein, G. H. 1964 *Nonsteady Flame Propagation*. Macmillan.

Matalon, M., Cui, C. & Bechtold, J. K. 2003 Hydrodynamic theory of premixed flames: effects of stoichiometry, variable transport coefficients and arbitrary reaction orders. *J. Fluid Mech.* **487**, 179–210.

Matalon, M. & Matkowsky, B. J. 1982 Flames as gasdynamic discontinuities. *J. Fluid Mech.* **124**, 239–259.

Michelson, D. M. & Sivashinsky, G. I. 1977 Nonlinear analysis of hydrodynamic instability in laminar flames – II. Numerical experiments. *Acta Astronautica* **4**, 1207–1221.

Palm-Leis, A. & Strehlow, R. A. 1969 On the propagation of turbulent flames. *Combust. Flame* **69**, 111–129.

Pelce, P. & Clavin, P. 1982 Influence of hydrodynamics and diffusion upon the stability limits of laminar premixed flames. *J. Fluid Mech.* **124**, 219–237.

Peskin, C. S. 1977 Numerical analysis of blood flow in the heart. *J. Comput. Phys.* **25**, 220–252.

Rahibe, O., Aubry, N. & Sivashinsky, G. I. 1998 Instability of pole solutions for planar propagating flames in sufficiently large domains. *Combust. Theory Modell.* **2**, 19–41.

Rastigejev, Y. & Matalon, M. 2006 Numerical simulation of flames as gasdynamic discontinuities. *Combust Theory Modell.* (to appear).

Sattler, S. S., Knaus, D. A. & Gouldin, F. C. 2002 Determination of three-dimensional flamelet orientation distributions in turbulent V-flames from two-dimensional image data. *Proc. Combust. Inst.* **29**, 1785–1792.

Sethian, J. A. 1996 *Level Set Methods and Fast Marching Methods*. Cambridge University Press.

Sivashinsky, G. I. 1977 Nonlinear analysis of hydrodynamic instability in laminar flames – I. Derivation of basic equations. *Acta Astronautica* **4**, 1177–1206.

Strehlow, R. A. 1984 *Combustion Fundamentals*. McGraw-Hill.

Thual, O., Frish, U. & Henon, M. 1985 Application of pole decomposition to an equation governing the dynamics of wrincled flame fronts. *J. Phys. Paris* **46**, 1485–1494.

Vaynblat, D. & Matalon, M. 2000*a* Stability of pole solutions for planar propagating flames: I. Exact eigenvalues and eigenfunctions. *SIAM J. Appl. Maths* **60**, 679–702.

Vaynblat, D. & Matalon, M. 2000*b* Stability of pole solutions for planar propagating flames: II. Properties of eigenvalues/eigenfunctions. *SIAM J. Appl. Maths* **60**, 702–728.